

Supplemental Material

Ultimate light trapping in free-form plasmonic waveguide

Juho Park,¹ Sanmun Kim,² Joongwon Lee,³ Sergey G. Menabde,^{1,*} and Min Seok Jang^{1,*}

¹*School of Electrical Engineering, KAIST, Daejeon 34141, Korea*

²*St. John's College, University of Cambridge, Cambridge, CB2 1TP United Kingdom*

³*School of Electrical and Computer Engineering, Cornell University, Ithaca, New York 14853, United States*

** menabde@kaist.ac.kr; * jang.minseok@kaist.ac.kr

S1. Transfer matrix formalism

In our work, we use the transfer matrix formalism to calculate the field distribution inside the waveguide. An MIM waveguide has two fundamental eigenmodes obtained from the solution of Maxwell's equations. We denote these eigenmodes as $|f\rangle$ and $|b\rangle$ where the letter f indicates “forward” (positive index) mode, having the direction of phase and energy velocities parallel to each other, and letter b indicates “backward” (negative index) mode, having antiparallel phase and energy velocities. Each eigenmode can propagate along either $+z$ or $-z$ direction, hence we further distinguish eigenmodes by their energy propagation direction by labelling with “+” and “-” signs. To sum up, there exist four plasmonic modes in a rainbow trapping MIM waveguide, indicated as $|f+\rangle$, $|f-\rangle$, $|b+\rangle$, and $|b-\rangle$.

In order to derive the dispersion relation, and obtain the field profiles for those four TM₂ modes, one can solve Maxwell's equations for planar MIM waveguide: $\nabla^2 \mathbf{H} + \omega \epsilon \mu_0 \mathbf{H} = 0$. Since we are considering TM modes, only the y -component of the magnetic field exists, which is assumed to have an exponential form (since we are solving for plasmonic waves):

$$H_y(x) = \begin{cases} Ae^{\gamma_2(x+\alpha)} & (x \leq -\alpha) \\ Be^{-\gamma_1 x} + Ce^{\gamma_1 x} & (|x| < \alpha) \\ De^{-\gamma_2(x-\alpha)} & (x \geq \alpha) \end{cases}$$

where $\gamma_1 = k_0 \sqrt{n_{\text{eff}}^2 - \epsilon_d}$, $\gamma_2 = k_0 \sqrt{n_{\text{eff}}^2 - \epsilon_m}$, $n_{\text{eff}} = \frac{\beta}{k_0}$ is the mode's effective index, k_0 is the free-space wavevector, α is the half of the core thickness, and A, B, C, D are the complex amplitudes to be solved for. Then, from the Maxwell's equations, we can directly obtain the electric field components: $E_x(x) = \frac{\beta}{\omega \epsilon} H_y$, $E_z(x) = \frac{i}{\omega \epsilon} \frac{\partial H_y}{\partial x}$. At the interface between the metal and insulator ($x = \pm\alpha$), H_y and E_z fields should be continuous. Under this boundary

condition, we obtain the complex amplitudes and a closed-form dispersion relation $n_{\text{eff}}(\omega)$ for the planar MIM waveguide:

$$e^{-2U} = \frac{U/\varepsilon_d + W/\varepsilon_m}{U/\varepsilon_d - W/\varepsilon_m}$$

where $U = \alpha k_0 \sqrt{n_{\text{eff}}^2 - \varepsilon_d} = \alpha \gamma_1$, and $W = \alpha k_0 \sqrt{n_{\text{eff}}^2 - \varepsilon_m} = \alpha \gamma_2$. Numerically solving the dispersion relation, we calculate the effective mode index n_{eff} for $|f + \rangle$, $|f - \rangle$, $|b + \rangle$, and $|b - \rangle$ modes, and obtain fields profile for each mode, starting with magnetic field:

$$H_y(x) = \begin{cases} e^{\gamma_2(x+\alpha)} & (x \leq -\alpha) \\ (e^{-\gamma_1 x} + e^{\gamma_1 x})/2 \cosh(\alpha \gamma_1) & (|x| < \alpha) \\ e^{-\gamma_2(x-\alpha)} & (x \geq \alpha) \end{cases}$$

Now, the four modes are normalized in order to apply the transfer matrix formalism. We normalize the field components of each eigenmode \mathbf{E}_m and \mathbf{H}_l by $\sqrt{|N_{ml}|} = \sqrt{|\int (\mathbf{E}_m \times \mathbf{H}_l + \mathbf{H}_m \times \mathbf{E}_l)_z / 4 dx|}$, which leads to the modes orthogonality condition:

$$\int (\mathbf{e}_m \times \mathbf{h}_l + \mathbf{h}_m \times \mathbf{e}_l)_z / 4 dx = \begin{cases} \frac{N_{ml}}{|N_{ml}|} & (m = l) \\ 0 & (m \neq l) \end{cases} \quad m, l = |f + \rangle, |f - \rangle, |b + \rangle, |b - \rangle,$$

where \mathbf{e}_m and \mathbf{h}_l are the normalized m^{th} electric and l^{th} magnetic field vectors. Note that the direction of x, y, z axis are identical to those in the main text.

To apply the transfer matrix formalism, we approximate the waveguide as a cascade of thin parallel waveguide segments (of constant thickness). There are two types of matrices involved in the transfer matrix method; one is the propagation matrix which accounts for the wave propagation in each waveguide segment, and the other is the interface matrix which accounts for the mode coupling at the interface of the neighboring waveguide segments. The propagation matrix for the m^{th} eigenmode at j^{th} thin parallel waveguide component is calculated as $T_{j,lm} = \delta_{lm} \exp(in_{\text{eff}} k_0 \Delta z)$, where Δz is the lateral length of the thin waveguide segment.

The interface matrix accounts for the mode coupling at the interface of the two neighboring waveguide segments since the change of the core thickness induces the change in the mode amplitude. This conversion is computed with butt-coupling coefficients in coupled-mode theory, which composes the elements in an interface matrix. The interface matrix between j^{th} and $(j+1)^{\text{th}}$ waveguide segments is given by:

$$S_{j,lm} = \frac{(\int(\mathbf{e}_l^{j+1} \times \mathbf{h}_m^j)_x dx + \int(\mathbf{e}_m^j \times \mathbf{h}_l^{j+1})_x dx)}{2 \int(\mathbf{e}_l^{j+1} \times \mathbf{h}_l^{j+1})_x dx}.$$

Here, \mathbf{e}_m^j and \mathbf{h}_m^j are the electric field and magnetic field vectors of the normalized m^{th} eigenmode in j^{th} waveguide segment.

To calculate the mode distribution inside the waveguide, we apply the boundary conditions such that the amplitude of $|f+\rangle$ is unity at the input, amplitude of $|b+\rangle$ mode is zero at the input, and the amplitudes of $|f-\rangle$ and $|b-\rangle$ modes disappear at the output. These boundary conditions reflect the fact that the $|b+\rangle$ mode cannot exist at the input because it is neither excited nor reflected, and that $|f-\rangle$ and $|b-\rangle$ modes cannot exist at the output for the same reason (see Figure 1 in the main text). By imposing the boundary conditions to the transfer matrices, the following system of equations for the complex mode amplitudes a are obtained:

$$\begin{bmatrix} a_{\text{out},f+} \\ 0 \\ a_{\text{out},b+} \\ 0 \end{bmatrix} = \prod S_i T_i \begin{bmatrix} 1 \\ a_{\text{in},f-} \\ 0 \\ a_{\text{in},b-} \end{bmatrix}.$$

Then, by applying the transfer matrix, we obtain the amplitudes at any j^{th} waveguide segment:

$$\begin{bmatrix} a_{j,f+} \\ a_{j,f-} \\ a_{j,b+} \\ a_{j,b-} \end{bmatrix} = \prod_{i=0}^{j-1} S_i T_i \begin{bmatrix} 1 \\ a_{\text{in},f-} \\ 0 \\ a_{\text{in},b-} \end{bmatrix}.$$

Therefore, total electromagnetic field in j^{th} waveguide segment $\mathbf{E}^j, \mathbf{H}^j$ can be expressed in terms of normalized eigenmodes and their amplitudes:

$$\mathbf{E}^j = a_{j,f+} \mathbf{e}_{f+}^j + a_{j,f-} \mathbf{e}_{f-}^j + a_{j,b+} \mathbf{e}_{b+}^j + a_{j,b-} \mathbf{e}_{b-}^j$$

$$\mathbf{H}^j = a_{j,f+} \mathbf{h}_{f+}^j + a_{j,f-} \mathbf{h}_{f-}^j + a_{j,b+} \mathbf{h}_{b+}^j + a_{j,b-} \mathbf{h}_{b-}^j$$

With known complex mode amplitudes and fields along the waveguide, we calculate the energy density u and the light trapping quality factor, maximized by the optimization algorithm via the modification of waveguide profile (as described in the main text).

S2. Optimization approach: details

We use three optimization methods, Genetic Algorithm (GA), Particle Swarm Optimization (PSO) and Bound Optimization BY Quadratic Approximation (BOBYQA) in optimization process [S1–S3]. We constructed our own code for GA, but for PSO and BOBYQA, Python library PySwarm [S4] and PyBOBYQA [S5,S6] were used. BOBYQA is a numerical optimization method based on the trust-region method. We utilize the derivative-free characteristic of the algorithm since deriving the analytic derivative of a quality factor along thickness α is not a trivial task. PSO is a pool-based algorithm as well as GA. This algorithm uses multi-particle to find the global optimum in the constraint region while sharing the best location of the entire swarm.

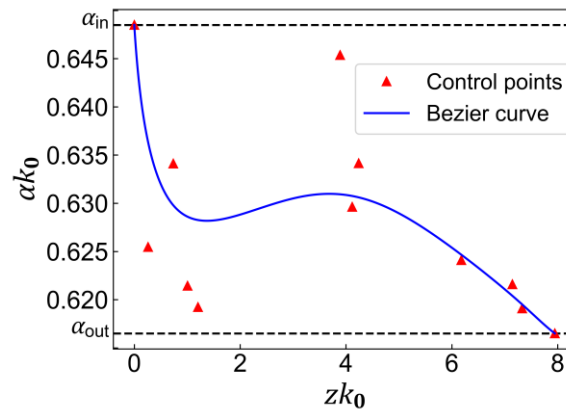


Figure S1. Bezier curve (blue line) based on the 10 control points (red triangles). Note that the input $(0, \alpha_{in})$ and output $(8, \alpha_{out})$ points are fixed, and therefore not counted as control points.

To model the waveguide core profile in a way suitable for optimization, we use Bezier curve which is built based on the set of control points, as shown in Figure S1. We used ten control points to model the waveguide core profile. The number of control points were empirically determined such that the quality factor converges at the fastest rate, since their number must be large enough to provide enough degrees of freedom to the Bezier curve (hence, the optimization). The same set of control points was used as an input for all three algorithms as well as the constraints on their coordinates allowed during the optimization. The points coordinates were limited as follows: x coordinate should be in the range $[0, L]$, where L is the length of the optimized waveguide, and y coordinate should be in the range $[\alpha_{out}, \alpha_{in}]$, where $\alpha_{out} = 0.616$ and $\alpha_{in} = 0.648$ are the semi-thickness of the core at the input and output ports, respectively (see the main text for details).

In the GA case, the coordinates of ten control points (x_i, y_i) acted as genes, and the Bezier curve created from these genes acted as a chromosome. In the selection-based operation of GA, a specific amount of superior chromosomes was selected based on its quality factor by the “roulette wheel” selection. Then, selected chromosomes created the next-generation chromosome pool through the crossover and mutation operations. Crossover operation was implemented such that genes in the newly created chromosome are the weighted sum of the genes in previously selected chromosomes: $(x_{\text{crossover}}, y_{\text{crossover}}) = \sum(w_i x_i, w_i y_i)$, where weights w_i form a uniform random distribution. Then, these genes were slightly modified by the mutation operation, where each gene $(x_{\text{crossover}}, y_{\text{crossover}})$ was mapped to $(x_{\text{mutation}}, y_{\text{mutation}}) = (x_{\text{crossover}} + \delta, y_{\text{crossover}} + \varepsilon)$. Here, δ and ε form a Gaussian distribution of $N(0, 0.001^2)$.

For the PSO case, we used an open-source Python library PySwarm. Further information about the algorithm itself can be found elsewhere. We set swarm size as 30. For BOBYQA, we used open-source Python library Py-BOBYQA. Optimization region bounds are identical to those used in PSO, and we utilized the software’s global optimum finding feature.

S3. Evidences for successful optimization

To check if our optimization successfully reached near the upper bound of the quality factor, we show two numerical simulations and provide a physical interpretation of the optimized quality factor. First, in order to check whether the optimum that we obtained is not on the path to the other local optimum with higher quality factor, we used the result obtained with PSO as an input to BOBYQA. Because BOBYQA is a trust-region-based method to find the local optimum near the initial input, the algorithm may converge to an optimum with a higher quality factor if the initial point is in the vicinity of it. However, the local optimum obtained with BOBYQA had almost the same quality factor and similar waveguide shape (Figure S2). This is a convincing evidence that the initial result (profile generated by PSO) is a local optimum.

Second, we calculated the quality factor of waveguide mixes, created from a pair of optimized waveguide profiles. The mixture profiles were constructed by linear mixing of the thickness of the two waveguides at same lateral position, with a mixing weight varying from zero to unity (i.e. migration from one profile to another). As shown in Figure S3, mixtures of all pairs exhibit lower quality factor compared to the original waveguide geometries. This shows the three optimized curves obtained from GA, PSO, and BOBYQA are in distinct local

optimum regions. Furthermore, the quality factors obtained from mixing the waveguides were the lowest in BOBYQA-GA pair. We speculate that the significant drawback in the quality factor is due to the larger difference between BOBYQA- and GA-generated geometries.

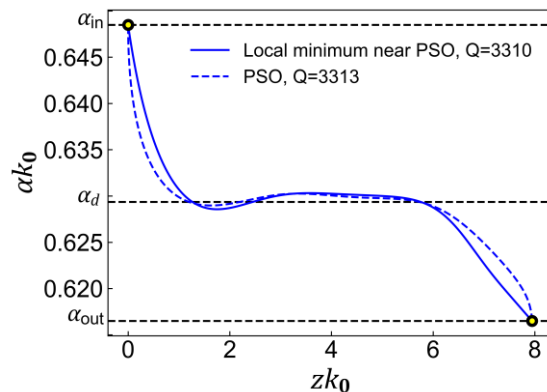


Figure S2. Input waveguide profile obtained from PSO (blue solid), and output waveguide profile achieved by BOBYQA (blue dotted) using the PSO-generated profile as an input.

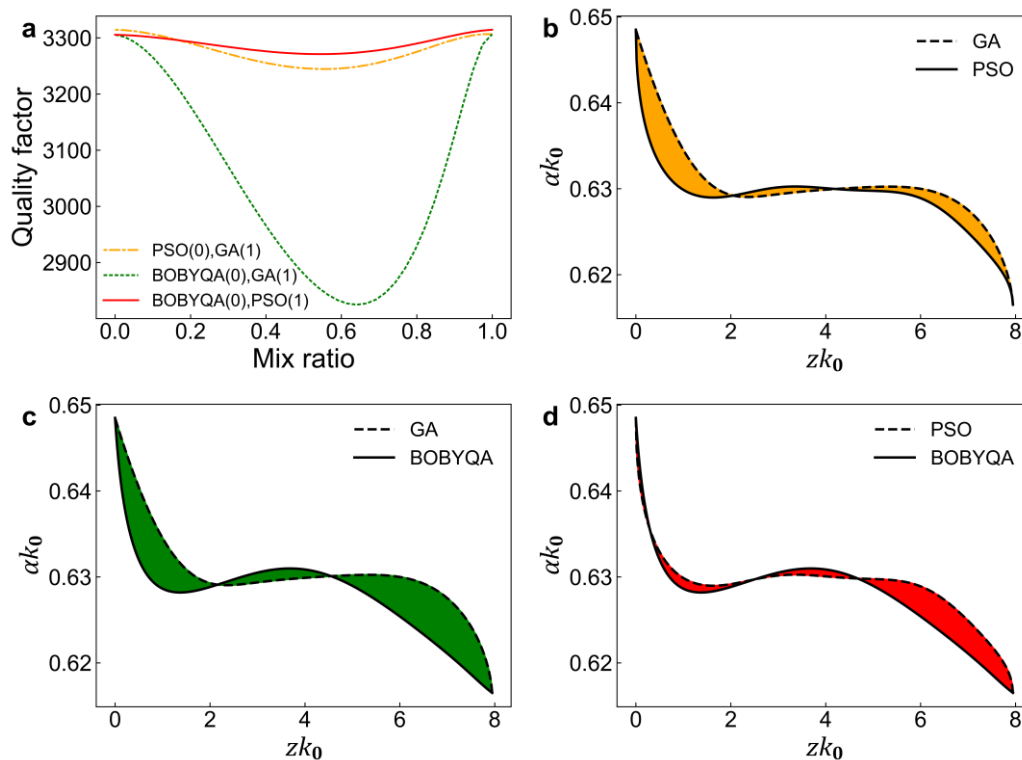


Figure S3. (a) Quality factor of mixed profiles as a function of mixing weight: PSO and GA (yellow dash-dotted), BOBYQA and GA (green dotted), BOBYQA and PSO (red solid). Mixed profiles are visualized as filled regions between the profile pairs being mixed: (b) PSO and GA (yellow), (c) BOBYQA and GA (green), (d) BOBYQA and PSO (red).

Finally, we verify that the achieved local optima are in the proximity of the theoretically limited upper bound Q_{ub} for the quality factor. We assume that the theoretical limit for the quality factor corresponds to the case when the incident $|f+\rangle$ mode propagates through an infinitely long parallel waveguide with its core thickness selected to maximize the ratio $\omega u/P$ between the time-averaged energy density u and the absorption loss P . We also confirmed that the maximum possible $\omega u/P$ for $|b+\rangle$ mode is much smaller than that for $|f+\rangle$ mode due to different field profile (in the MIM case, larger part of the $|b+\rangle$ mode resides in the metal, hence the negative index, leading to a higher Ohmic loss). Note that $\omega u/P$ is constant along the parallel waveguide, so calculating $\omega u/P$ only for the cross-section at given core thickness is sufficient. $\omega u/P$ for $|f+\rangle$ mode as a function of the core thickness is shown in the Figure S4(a), and $Q_{ub} = \max\{\omega u/P\}$. Optimized light trapping quality factor Q_{opt} is as close to the upper bound as 99%, confirming the successful optimization (Figure S4(b)).

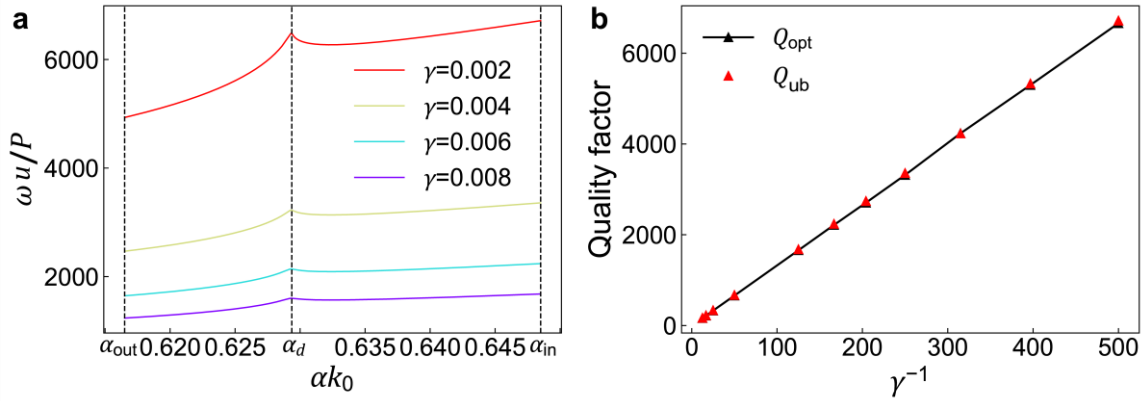


Figure S4. (a) $\omega u/P$ as a function of waveguide thickness for different metal loss γ . (b) Optimized quality factor Q_{opt} as a function of metal loss γ for the segment of length $Lk_0 = 8$ (black solid line and triangles) and theoretical upper bound Q_{ub} (red triangles).

S4. Number of control points for Bezier curve

We optimized the system for different number of control points from 1 to 20 in order to analyze the importance of the number of points for the optimization performance. The results (Figure S5) show that the optimized quality factor is practically insensitive to the number of control points starting with three: the difference between the maximum and minimum values is only about 0.1%. Two control points failed to achieve high quality factor, with the best result at least 40% lower than that using three points. Therefore, we conclude that using as few as three control points is enough to reach the best possible optimization results.

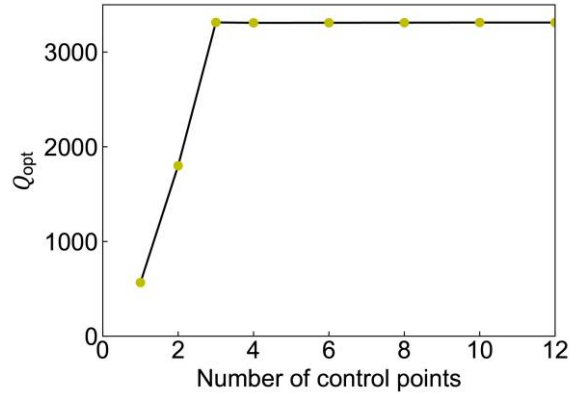


Figure S5. Optimized quality factor Q_{opt} (data points) as a function of number of control points for Bezier curve. Data obtained with transfer matrix method.

S5. Logarithmic scaling law of the quality factor in IMI structure

To support our argument on the relationship between the metal loss γ , the characteristic length L_c , and the optimized quality factor Q (from now, we treat Q as Q_{opt} since we focus on optimized quality factors), we conducted the same optimization process to IMI structure. We set input and output core thickness as $ak_0 = 0.0282$ and 0.0298 respectively. The input and output thicknesses were selected to include the degeneracy point (similar to the MIM case described in the main text). The dielectric permittivities of the insulator and metal were set the same as for MIM structure: $\epsilon_d = 10$ and $\epsilon_m = -2 + \gamma i$. IMI TM_0 $|f + \rangle$ mode was used as an incident one and we imposed the identical boundary conditions as in the MIM case: amplitude of the $|b + \rangle$ mode at the input, and $|f - \rangle$ and $|b - \rangle$ modes at the output were set to zero. The set of optimization processes was conducted for the different metal losses ranging from $\gamma = 0.002$ to $\gamma = 0.02$, and the waveguide lengths were swept between $Lk_0 = 0.1$ and $Lk_0 = 15$. However, we used slightly different optimization settings for the IMI waveguide: six control points were used to model the core profile, and the GA was iterated for 300 epochs since it converged at slower rate compared to the MIM case.

The optimization results for different sets of parameters are shown in Figure S6. Most importantly, the relationship between optimized Q and γ^{-1} is linear at sufficiently long length, same as in MIM structure. Furthermore, the characteristic length L_c scales with $\log(\gamma^{-1})$, also similar to the MIM case. Therefore, we speculate that observed relationships for $Q(\gamma^{-1})$ and $L_c(\gamma^{-1})$ are not restricted to MIM structure, but general for all free-form plasmonic waveguides.

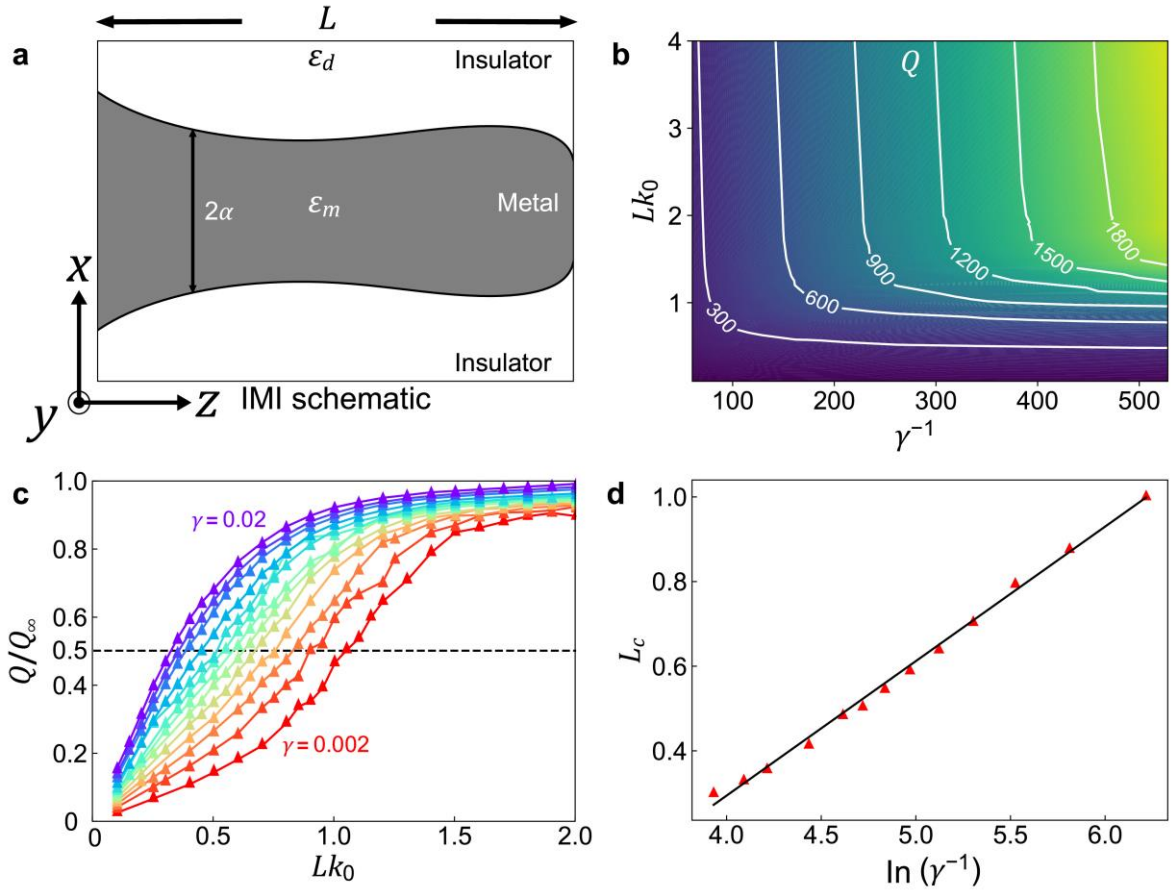


Figure S6. (a) Schematics of a free-form IMI light trapping plasmonic waveguide; the curvature is exaggerated. (b) Optimized quality factor as a function of the waveguide length L and metal loss γ . (c) Normalized quality factor Q/Q_∞ as a function of L for different loss values. (d) Characteristic length L_c versus the logarithm of inverse metal loss (data points; solid line is the least-square linear fit). All data obtained with the transfer matrix method.

S6. Discussion on quality factor to mode volume ratio

We calculate effective mode volume V_{eff} as a measure of spatial light trapping capability. Effective mode volume V_{eff} can be calculated as $V_{\text{eff}} = A_{\text{eff}}L_y$, where $A_{\text{eff}} = U/\max\{u(x,z)\}$ is the effective mode area, and L_y is the diffraction-limited transverse length; $L_y = \lambda_0/2n_d$. Figure S7 shows Q/V_{eff} as a function of waveguide length L . For all considered loss γ , Q/V_{eff} has its maximum at a certain waveguide length. Considering that Q saturates and A_{eff} inherently increases along L , $\max\{Q/V_{\text{eff}}\}$ can be interpreted as an optimal balance between the spatial and temporal light localization.

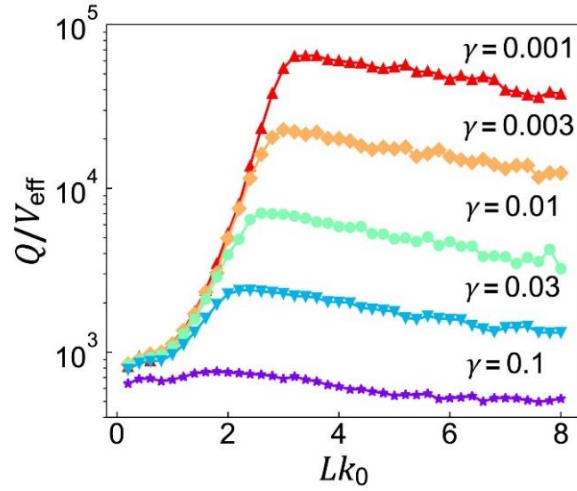


Figure S7. The ratio of quality factor Q to mode volume V_{eff} , normalized by $(\lambda_0/n_d)^{-3}$.

S7. Optimization examples using realistic materials

For the visible frequency range, we choose the free-space wavelength of 400 nm. In this frequency range, it is difficult to find materials with permittivity values that satisfy the existence condition for both positive and negative index TM_2 mode in the MIM waveguide, which provides efficient light trapping. We select TiO_2 ($\epsilon \approx 7.09 + 0.002i$) [S7] for the dielectric and single-crystal Ag ($\epsilon \approx -1.7 + 0.15i$) [S8] for metal layer. Single-crystal Ag [S8] exhibits small loss compared to the bulk silver, due to the lower number of impurities. Using these materials, we optimized the waveguide having the input port thickness $\alpha_{\text{in}} = 53.5$ nm, output port thickness $\alpha_{\text{out}} = 42.86$ nm, and length $L = 154.7$ nm. Input and output port thicknesses are selected to have the degeneracy value between them. Obtained waveguide profile shows quality factor of $Q = 82.3$, which is 2.2 times higher compared to that of the linearly tapered waveguide $Q = 37.1$ under similar conditions. The profile of this waveguide is shown in Figure S8(a). However, as becomes evident from the profile plot, the nanometer-scale dimensions of this waveguide are not feasible for fabrication.

To increase the overall size of the waveguide, we conduct another optimization, selecting the free-space wavelength of 11 μm in a widely used mid-IR frequency range. At this wavelength, several dielectric materials (Si, GaAs, Ge, ZnSe, etc.) exhibit very low loss and large real part of permittivity; we use Ge ($\epsilon \approx 16.01$) which has negligible loss at selected frequency [S9]. As metal, we use polar dielectric SiC ($\epsilon \approx -3.8 + 0.125i$), employing its reststrahlen phonon bands [S10-S12] where the real part of permittivity satisfies the necessary TM_2 existence conditions.

Using these materials at mid-IR frequency, we optimized the waveguide having the input port thickness $\alpha_{\text{in}} = 0.985 \mu\text{m}$, output port thickness $\alpha_{\text{out}} = 0.784 \mu\text{m}$, and length $L = 2.6 \mu\text{m}$. As in the previous case, input and output ports thicknesses are calculated to enclose the degeneracy point between them. Obtained waveguide profile shows quality factor of $Q = 198.7$, which is 5.2 times higher compared to that of the linearly tapered waveguide $Q = 38.2$ under similar conditions. The profile of this waveguide is shown in Figure S8(b). In this case, the geometrical dimensions are in micrometer-scale range, and the curvature of the core is smooth enough to be fabricated by modern methods: thickness changes by $\approx 100 \text{ nm}$ along the $1 \mu\text{m}$ segment.

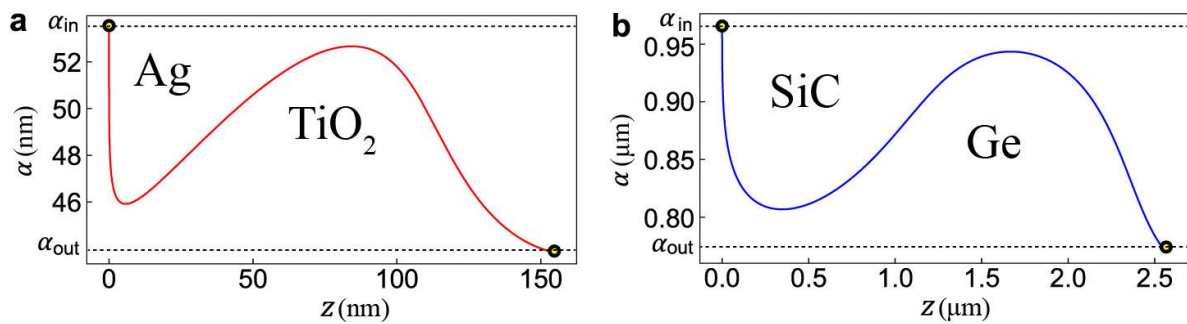


Figure S8. Waveguide profile obtained as a semi-realistic demonstration, (a) at 400 nm free-space wavelength, using TiO_2 and single-crystal Ag as dielectric and metal layer respectively, (b) at 11 μm free-space wavelength, using SiC and Ge as metal and dielectric layer respectively.

References

- [S1] K. Deb, Multi-Objective Optimization Using Evolutionary Algorithms (John Wiley & Sons, Inc., New York, NY, USA, 2001).
- [S2] Eberhart and Yuhui Shi, Particle swarm optimization: developments, applications and resources, in Proc. 2001 Congr. Evol. Comput. (IEEE Cat. No.01TH8546) (IEEE, 2001), pp. 81–86.
- [S3] M. J. D. Powell, The BOBYQA algorithm for bound constrained optimization without derivatives, Cambridge NA Rep. NA2009/06, Univ. Cambridge, Cambridge 26 (2009).
- [S4] L. James V. Miranda, PySwarms: a research toolkit for Particle Swarm Optimization

- in Python, *J. Open Source Softw.* **3**, 433 (2018).
- [S5] C. Cartis, L. Roberts, and O. Sheridan-Methven, Escaping local minima with derivative-free methods: a numerical investigation, Eprint ArXiv:1812.11343 arXiv:1812.11343 (2018).
- [S6] C. Cartis, J. Fiala, B. Marteau, and L. Roberts, Improving the Flexibility and Robustness of Model-Based Derivative-Free Optimization Solvers, Eprint ArXiv:1804.00154 arXiv:1804.00154 (2018).
- [S7] T. Siefke, S. Kroker, K. Pfeiffer, O. Puffky, K. Dietrich, D. Franta, I. Ohlidal, A. Szeghalmi, E.-B. Kley, and A. Tunnermann, Materials pushing the application limits of wire grid polarizers further into the deep ultraviolet spectral range, *Adv. Opt. Mater.* **4**, 1780 (2016).
- [S8] T. Mori, T. Mori, M. Fujii, Y. Tominari, A. Otomo, and K. Yamaguchi, Optical Properties of Low-Loss Ag Films and Nanostructures on Transparent Substrates, *ACS Appl. Mater. Interfaces* 2018, **10**, 8333 (2018).
- [S9] H. H. Li, Refractive Index of Silicon and Germanium and Its Wavelength and Temperature Derivates, *Journal of Physical and Chemical Reference Data* **9**, 561 (1980).
- [S10] J. D. Caldwell, L. Lindsay, V. Giannini, I. Vurgaftman, T. L. Reinecke, S. A. Maier, and O. J. Glembocki, Low-loss, infrared and terahertz nanophotonics using surface phonon polaritons, *Nanophotonics* **4**, 44 (2015).
- [S11] J. D. Caldwell, G. J. Orest, Y. Francescato, N. Sharac, V. Giannini, F. J. Bezares, J. P. Long, J. C. Owrutsky, I. Vurgaftman, J. G. Tischler, V. D. Wheeler, N. D. Bassim, L. M. Shirey, R. Kasica, and S. A. Maier, Low-Loss, Extreme Subdiffraction Photon Confinement via Silicon Carbide Localized Surface Phonon Polariton Resonators, *Nano Lett.* **13**, 3690 (2013).
- [S12] R. Hillenbrand, T. Taubner, and F. Keilmann, Phonon-enhanced light-matter interaction at the nanometre scale, *Nature* **418**, 159 (2002).